Title

High-Energy-Density Asymmetric Supercapacitor Based on Free-Standing Ti3C2T X @NiO-Reduced Graphene Oxide Heterostructured Anode and Defective Reduced Graphene Oxide Hydrogel Cathode

Journal

ACS Applied Materials & Interfaces, 14(17)

ISSN

1944-8244

Authors

Chen, Weiwen

Hao, Chunfeng

Qiu, Zenghui

et al.

Publication Date

2022-05-04

DOI

10.1021/acsami.2c02507

ACS APPLIED MATERIALS & INTERFACES

www.acsami.org

Research Article

High-Energy-Density Asymmetric Supercapacitor Based on Free-Standing $Ti_3C_2T_X$@NiO-Reduced Graphene Oxide Heterostructured Anode and Defective Reduced Graphene Oxide Hydrogel Cathode

Weiwen Chen, Chunfeng Hao, Zenghui Qiu,* Xin Zhang, Haijun Xu,* Bingzhe Yu, and Shaowei Chen*

Cite This: *ACS Appl. Mater. Interfaces* 2022, 14, 19534–19546

Read Online

ACCESS | Metrics & More | Article Recommendations | Supporting Information

ABSTRACT: The rational design of an asymmetric supercapacitor (ASC) with an expanded operating voltage window has been recognized as a promising strategy to maximize the energy density of the device. Nevertheless, it remains challenging to have electrode materials that feature good electrical conductivity and high specific capacitance. Herein, a 3D layered $Ti_3C_2T_X$@NiO-reduced graphene oxide (RGO) heterostructured hydrogel was successfully synthesized by uniform deposition of NiO nanoflowers onto $Ti_3C_2T_X$ nanosheets, and the heterostructure was assembled into a 3D porous hydrogel through a hydrothermal GO-gelation process at low temperatures. The resultant $Ti_3C_2T_X$@NiO-RGO heterostructured hydrogel exhibited an ultrahigh specific capacitance of 979 F g^{-1} at 0.5 A g^{-1}, in comparison to that of $Ti_3C_2T_X$@NiO (623 F g^{-1}) and $Ti_3C_2T_X$ (112 F g^{-1}). Separately, a defective RGO (DRGO) hydrogel was found to exhibit a drastic increase in specific capacitance, compared to untreated RGO (261 vs 178 F g^{-1} at 0.5 A g^{-1}), owing to abundant mesopores. These two materials were then used as free-standing anode and cathode to construct an ASC, which displayed a large operating voltage (1.8 V), a high energy density (79.02 Wh kg^{-1} at 450 W kg^{-1} and 45.68 Wh kg^{-1} at 9000 W kg^{-1}), and remarkable cycling stability (retention of 95.6% of the capacitance after 10,000 cycles at 10 A g^{-1}). This work highlights the unique potential of $Ti_3C_2T_X$-based heterostructured hydrogels as viable electrode materials for ASCs.

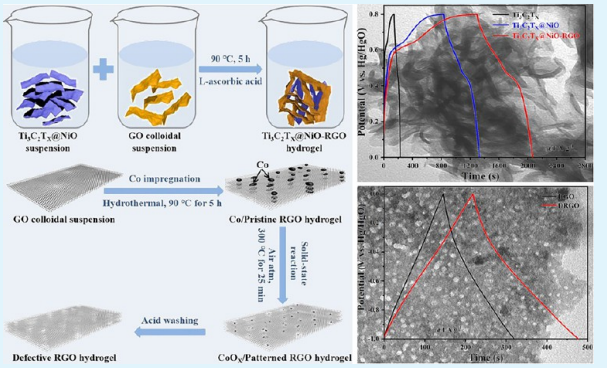

KEYWORDS: *$Ti_3C_2T_X$ heterostructure, hydrogel, graphene oxide, high energy density, asymmetric supercapacitor*

1. INTRODUCTION

Electrochemical capacitors, also called supercapacitors (SCs), have been hailed as a viable technology for efficient energy storage that features an ultrahigh power density (10 to 10^4 W kg^{-1}), outstanding cycling stability (an ultralong cycle life over 10^5 cycles), and fast charging/discharging, and have found diverse applications in transportation, electronics, etc.[1−3] Yet, widespread application of SCs is hampered by the limited energy capacity.[4−7] Thus, extensive research has been carried out to maximize the energy density of SCs.

There are three types of SCs on the basis of the charge storage mechanisms, electric double-layer capacitors (EDLCs), pseudocapacitors, and asymmetric supercapacitors (ASCs). EDLCs store and release charges via facile adsorption/desorption of electrolyte ions at the electrode double layer,[4] whereas for pseudocapacitors, energy is stored through a fast reversible faradic process that may occur on and in the electrode materials.[1−3,5−7] ASCs refer to the devices in which one battery-type electrode acts as the anode while the cathode is a capacitor-type electrode.[1−3] Because of the different voltage windows of the anode/cathode, the operating voltage of the ASCs can be significantly widened, and the energy and power densities maximized.

2D transition-metal carbides/nitrides/carbonitrides (MXenes) have emerged as viable materials for ASC electrodes.[8,9] For instance, $Ti_3C_2T_X$ has attracted great attention for ASC anodes particularly owing to its high metallic conductivity, excellent hydrophilicity, adjustable layer spacing, and rich redox-active sites.[10,11] In fact, $Ti_3C_2T_X$ electrodes have displayed a high-rate performance, high power density, excellent cycling stability, and high energy density.[9,12] Nevertheless, there are two major challenges with pristine $Ti_3C_2T_X$. First, the terminal functional groups and surface defects formed in sample preparation may limit the specific charge storage capacity.[13] Second, the strong van der

Received: February 11, 2022
Accepted: April 12, 2022
Published: April 21, 2022

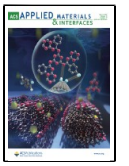

Waals interactions between delaminated $Ti_3C_2T_X$ nanosheets can result in aggregation, which vastly reduces the specific surface area and limits ionic dynamic diffusion.[14] To mitigate these issues, one effective strategy is to fabricate $Ti_3C_2T_X$-based heterostructures that combine the advantages of $Ti_3C_2T_X$ and pseudocapacitve materials.[15,16] The abundant surface functional groups/defects and unique 2D hierarchical structure of $Ti_3C_2T_X$ render it possible to construct desired synergetic heterostructures with excellent structural stability,[17,18] high specific capacitance, and excellent electrical conductivity.[19] For instance, low-cost, stable NiO features an ultrahigh theoretical specific capacitance of 3750 F g^{-1} and is viewed as an attractive option to form heterostructures with $Ti_3C_2T_X$.[20] To prevent self-stacking, one viable option is to integrate the hierarchical $Ti_3C_2T_X$@NiO heterostructures into a 3D interlinked framework,[21,22] which can also produce abundant active sites and facile ion/electron transfer pathways to significantly enhance the electrochemical kinetics.[21,23] One method is to take advantage of the self-gelation of reduced graphene oxide (RGO) into a 3D mesoporous hydrogel that can be composited with various active materials to produce SC electrodes.[24,25]

For ASCs, selection of the cathode materials is also important, which generally entail carbon derivatives, most notably graphene.[26,27] Yet, the aggregation of graphene nanosheets and the intrinsically narrow ion/electron transport channels are known to compromise the capacitance characteristics. One effective strategy to mitigate the issue is defect engineering.[28,29] For instance, patterning on graphene surfaces can be exploited to produce a mesoporous structure, leading to abundant pathways for ion penetration and hence improved storage capacity.[30,31] Furthermore, to minimize aggregation, the resultant defective RGO (DRGO) can be assembled into a 3D interconnected framework via self-gelation.[32]

In this study, a 3D layered $Ti_3C_2T_X$@NiO-RGO heterostructured hydrogel is fabricated by a simple, two-step strategy and used as an anode for ASCs. In the first step, a layered $Ti_3C_2T_X$@NiO heterostructure is synthesized through a liquid-phase deposition and thermal annealing procedure. Subsequently, the $Ti_3C_2T_X$@NiO heterostructure is assembled into a 3D mesoporous and conductive hydrogel by a low-temperature GO-assisted self-convergence hydrothermal strategy. Separately, a 3D DRGO hydrogel is prepared and used as a cathode for ASCs. Due to the high mechanical property of the 3D hydrogel structure, the obtained anode and cathode materials are fabricated directly without binders. A $Ti_3C_2T_X$@NiO-RGO//DRGO ASC is then constructed, which features a large operating voltage of 1.8 V, a 79.02 Wh kg^{-1} maximum energy density at 450 W kg^{-1} power density, along with excellent cycle stability (retention of 95.6% of the capacitance over 10,000 cycles).

2. EXPERIMENTAL SECTION

2.1. Sample Preparation. *2.1.1. $Ti_3C_2T_X$ MXene.* The Ti_3AlC_2 MAX-phase powder precursor was prepared by ball-milling a mixture of aluminum (Al), graphite (C), and TiH_2 (molar ratio 3:1.2:2) for 20 h using zirconia balls. The mixture was then heated at 1350 °C under an Ar atmosphere for 2 h.

$Ti_3C_2T_X$ was delaminated by following a classical etching process where the Al layers were selectively etched from the Ti_3AlC_2 MAX-phase precursor (<38 μm).[11] In brief, into 20 mL of a 9 M HCl solution was added 1 g of LiF and 1 g of Ti_3AlC_2 powders under magnetic stirring for 30 min in an ice bath before being heated at 40 °C for 38 h.[8] The resultant clay-like $Ti_3C_2T_X$ was separated by centrifugation at 3500 rpm and rinsed repeatedly with DI water and absolute alcohol. The obtained product was then sonicated in an Ar atmosphere, and the dark green supernatant was separated by centrifugation (3500 rpm, 30 min) to afford delaminated $Ti_3C_2T_X$ floccules.

2.1.2. $Ti_3C_2T_X$@NiO Heterostructures. Layered $Ti_3C_2T_X$@NiO heterostructures were synthesized by liquid-phase deposition along with thermal annealing. Typically, 1 g of the $Ti_3C_2T_X$ obtained above was dispersed into a 400 mL suspension containing $NiO(NO_3)_2 \cdot 6H_2O$ (3.88 g) and urea (16.06 g) under ultrasonication for 1 h to form a uniform solution. The mixture was heated at 90 °C for 3 h in an oil bath under continuous stirring, and the product was collected via centrifugation at 10,000 rpm, rinsed repeatedly with DI water and ethanol, and freeze-dried. This precursor was converted into $Ti_3C_2T_X$@NiO by thermal annealing at 350 °C for 2.5 h at a slow rate of 2 °C min^{-1}. Pristine NiO was prepared as a control in the same manner but in the absence of $Ti_3C_2T_X$.

2.1.3. $Ti_3C_2T_X$@NiO-RGO Heterostructured Hydrogel. The modified Hummers' method was used to synthesize GO from graphite flakes,[33,34] and a homogeneous colloidal suspension (2 mg mL^{-1}) was obtained by sonicating GO in water for 6 h, and the thin-layer components were separated by centrifugation (4000 rpm, 40 min). $Ti_3C_2T_X$@NiO particles (12 mg) were then dissolved in 1.5 mL of the prepared GO colloidal solution under mechanical stirring and sonication for 60 min to produce a homogeneous suspension, into which was immediately added 6 mg of L-ascorbic acid (GO/L-ascorbic acid mass ratio 1:2). After hydrothermal treatment at 90 °C for 6 h, $Ti_3C_2T_X$@NiO-RGO heterostructured hydrogel was produced, which was rinsed with DI water five to six times until pH was around neutral. As a control, an RGO hydrogel was synthesized in the same manner but without the addition of $Ti_3C_2T_X$@NiO composites.

2.1.4. 3D DRGO Hydrogel. 3D DRGO hydrogel was prepared hydrothermal, followed by cobalt (Co)-catalyzed gasification in ambient atmosphere. First, a certain amount of Co particles was diffused into 1.5 mL of the obtained GO (2 mg mL^{-1}) colloidal suspension under vigorous stirring and ultrasonication for 1 h to achieve a uniform GO/Co (10 wt %) hybrid dispersion, into which was added 6 mg of L-ascorbic acid (GO/L-ascorbic acid mass ratio 1:2) under mechanical stirring for 1 h, and the resultant suspension was treated hydrothermally at 90 °C for 5 h to obtain a 3D RGO hydrogel with Co particles attached uniformly on the surface. The resulting RGO/Co hybrid hydrogel was then rinsed with DI water repeatedly until pH ≈ 7 and collected by lyophilization, before oxidation in ambient atmosphere at 300 °C for 0.5 h. The sample was then soaked in a boiling 98% nitric acid solution for 60 min to remove cobalt oxide. Finally, the 3D DRGO hydrogel was rinsed extensively with water and freeze-dried. As a control, a 3D RGO hydrogel was prepared similarly but without the addition of Co particles.

2.2. Sample Structures. Transmission electron microscopy (TEM), energy-dispersive X-ray analysis (EDX), and selected area electron diffraction (SAED) studies were conducted with a Tecnai G2 F20 (200 kV), and field emission scanning electron microscopy (FE-SEM) was performed with a Hitachi S-4800 microscope (15 kV, 10 μA). X-ray photoelectron spectroscopy (XPS) studies were performed with a Thermo Fisher Escalab 250 spectrometer. X-ray diffraction (XRD) analysis was conducted with a Bruker D8 Advanced X-ray diffractometer (λ = 1.54 Å). Raman spectroscopic measurements were carried out with a micro-Raman spectrometer (laser excitation wavelength 532 nm). Thermal measurements were performed via thermogravimetric analysis (TGA). Nitrogen adsorption/desorption studies were conducted with an automatic adsorption instrument (Micromeritics, ASAP2020), where the Brunauer–Emmett–Teller (BET) method was used to estimate the specific surface area, whereas the desorption branch of the isotherm was used to produce the pore size distribution via the Barret–Joyner–Halenda (BJH) theory.

2.3. Electrochemistry. Electrochemical measurements were conducted in 1 M KOH in a conventional three-electrode configuration with a CHI 660C electrochemical workstation, a Hg/HgO reference electrode, and a Pt foil counter electrode. In the working electrode, the $Ti_3C_2T_X$ or $Ti_3C_2T_X$@NiO heterostructures

https://doi.org/10.1021/acsami.2c02507
ACS Appl. Mater. Interfaces 2022, 14, 19534−19546

were used as the active materials, which were prepared by pressing a uniform paste including heterostructures, poly(tetrafluoroethylene) (PTFE), and carbon black (mass ratio 80:10:10) onto a 1 cm × 1 cm Ni foam current collector. Owing to the excellent mechanical property, the 3D RGO, DRGO, and $Ti_3C_2T_X$@NiO-RGO hydrogel working electrodes were used in the absence of binders, with a loading of ca. 1.0 mg active materials. The working electrode was desiccated in vacuum at 90 °C for 12 h, before being immersed in an aqueous solution of 1 M KOH for 1 day to reach an equilibrium with the electrolyte.

2.4. ASC Device. The $Ti_3C_2T_X$@NiO-RGO//DRGO ASC was constructed using $Ti_3C_2T_X$@NiO-RGO as the anode, DRGO as the cathode, and 1 M KOH electrolyte. The performance was examined in a three-electrode setup. The mass ratio of $Ti_3C_2T_X$@NiO-RGO and DRGO was optimized by balancing the anode and cathode charges.[35]

3. RESULTS AND DISCUSSION

3.1. $Ti_3C_2T_X$@NiO-RGO Anode. Figure 1a shows the synthetic process for the layered $Ti_3C_2T_X$@NiO heterostructures, where the $Ti_3C_2T_X$ surface was decorated uniformly with $Ni(OH)_2$ nanosheets, and the resulting $Ti_3C_2T_X$@$Ni(OH)_2$ was thermally treated in air to produce layered $Ti_3C_2T_X$@NiO heterostructures. TEM measurements were first performed to examine the sample structures. From Figure 1b, the $Ti_3C_2T_X$ nanosheets can be seen to exhibit a 2D wrinkled paper-like structure, and in the $Ti_3C_2T_X$@NiO heterostructure, the $Ti_3C_2T_X$ surface is homogeneously covered with NiO nanoflowers with ultrathin nanopetals (Figure 1c,d). In HRTEM measurements (Figure 1e), the NiO nanopetals displayed clearly resolved lattice fringes, and the interplanar spacing of 0.21 nm is in good agreement with the NiO (200) crystalline planes (JCPDS 43-1477). The corresponding SAED patterns (Figure 1e, inset) show three bright rings due, respectively, to the (111), (200), and (220) crystalline planes of NiO. Moreover, one can see from Figure 1e that the hierarchical $Ti_3C_2T_X$@NiO composites feature a tight face-to-face contact between the two components, leading to excellent mechanical strength and electrochemical performance, as observed below.

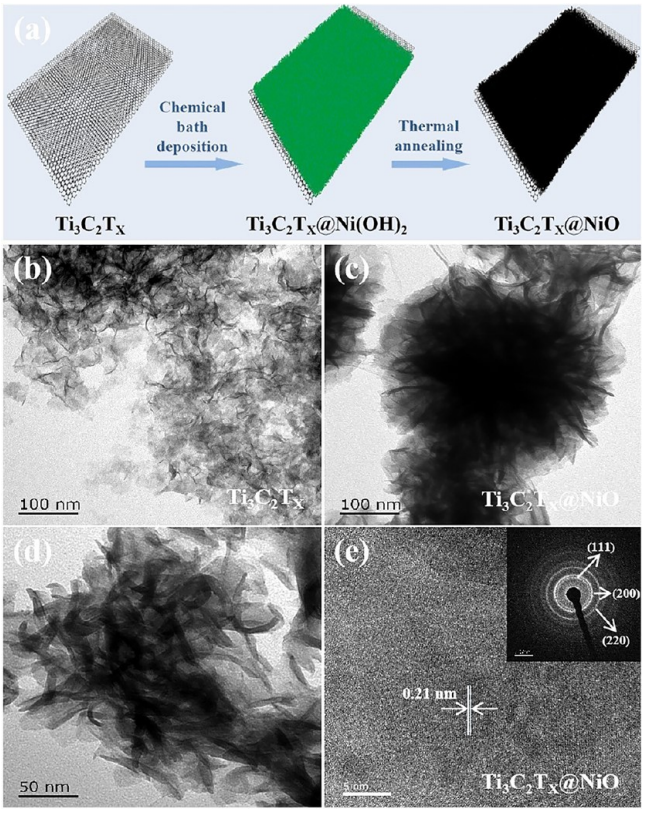

Figure 1. (a) Schematic illustration of the synthesis of hierarchical $Ti_3C_2T_X$@NiO heterostructures. TEM micrographs of (b) $Ti_3C_2T_X$ and (c, d) $Ti_3C_2T_X$@NiO. (e) Representative HRTEM image of $Ti_3C_2T_X$@NiO, with the corresponding SAED patterns in the inset.

Additional structural insights were produced in spectroscopic measurements. From the EDX data (Figure 2a), the elements of C, Ni, Ti, and O can be clearly observed and exhibit a rather even distribution within the sample, confirming good combination of NiO with $Ti_3C_2T_X$. Figure 2b shows the XRD patterns. $Ti_3C_2T_X$ (black curve) displays six strong peaks at 2θ = 6.5, 15.6, 24.9, 36.1, 40.9, and 58.1°, respectively, due to the (002), (004), (006), (111), (200), and (110) crystalline planes,[8] whereas three diffraction peaks can be seen at 2θ = 37.2, 43.2, and 62.8° for NiO (red curve), consistent with the NiO (111), (200), and (220) crystalline planes (JCPDS 43-1477). These diffraction features are all obviously observed in the $Ti_3C_2T_X$@NiO composites (blue curve); yet the (002) peak of $Ti_3C_2T_X$@NiO appears at a smaller angle than that of $Ti_3C_2T_X$, indicating that coverage of NiO on the $Ti_3C_2T_X$ surface suppresses the self-stacking of $Ti_3C_2T_X$. Moreover, no obvious characteristic peaks of $Ni(OH)_2$ can be resolved, confirming that the symmetrical Ni−OH was converted into Ni−O thoroughly in the thermal annealing process.

In Raman measurements (Figure 2c), it can be seen that both $Ti_3C_2T_X$ and $Ti_3C_2T_X$@NiO displayed the characteristic peaks at 203, 316, 464, 664, and 732 cm^{-1}, corresponding to the Ti-C vibrations of $Ti_3C_2T_X$.[11] Meanwhile, two additional broad peaks appeared at 566 and 1068 cm^{-1}, due, respectively, to the first-order phonon (1P) and second-order phonon (2P) scattering of NiO and $Ti_3C_2T_X$@NiO heterostructures. The fact that no other peak is detected confirms that the NiO nanoflowers were evenly deposited on the $Ti_3C_2T_X$ nanosheet surface.

The elemental composition and valency of the materials were then investigated by XPS measurements. In the survey spectra (Figure 3a,b), the C 1s, Ti 2p, and O 1s electrons can be found at ca. 286, 459, and 530 eV for $Ti_3C_2T_X$ and $Ti_3C_2T_X$@NiO heterostructures. An additional peak (ca. 856 eV), consistent with Ni 2p, appears after NiO deposition on the $Ti_3C_2T_X$ surfaces, suggesting the successful preparation of the heterostructure (Figure 1a). Figure 3c−f shows the high-resolution scans of the C 1s, Ti 2p, O 1s, and Ni 2p electrons of $Ti_3C_2T_X$@NiO composites. In the C 1s scan (Figure 3c), four peaks are resolved: C−Ti at 281.1 eV, C−C at 284.5 eV, C−O at 285.5 eV, and C═O at 288.6 eV.[26] Figure 3d displays the Ti 2p spectrum which entails two doublets at 454.6/461.2 and 458.8/464.6 eV, attributable to the $2p_{3/2}/2p_{1/2}$ electrons of Ti-C and Ti-O, respectively.[28] When NiO was deposited onto the $Ti_3C_2T_X$ nanosheets, the amount of functional groups decreased and partial oxidation diminished. From the O 1s scan (Figure 3e), two subpeaks are deconvoluted, Ni−O at 530.1 eV and C−Ti−O at 531.9 eV, and the Ni 2p scan (Figure 3f) consists of a doublet at 853.7/855.6 eV that can be attributed to the Ni^{2+} $2p_{3/2}/2p_{1/2}$ electrons, consistent with the formation of NiO.[15]

The $Ti_3C_2T_X$@NiO composites were then assembled into a 3D porous RGO hydrogel using GO as a gelation agent (Figure 4a) under low-temperature hydrothermal treatment to

https://doi.org/10.1021/acsami.2c02507
ACS Appl. Mater. Interfaces 2022, 14, 19534−19546

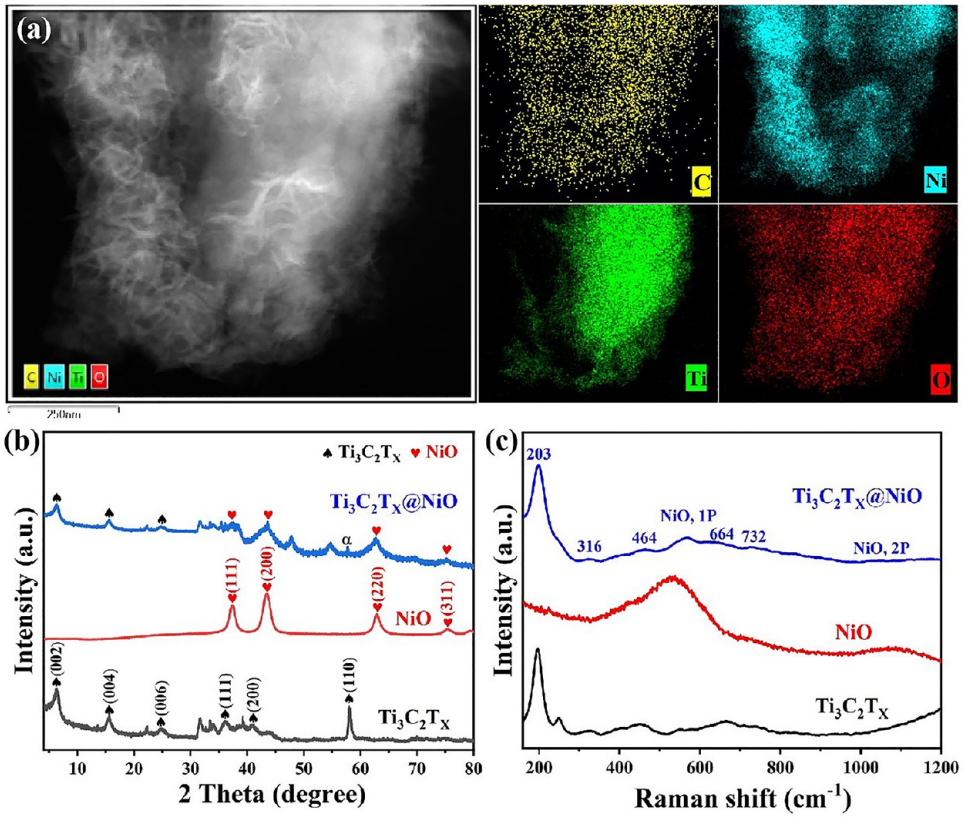

Figure 2. (a) TEM micrograph of the $Ti_3C_2T_X$@NiO heterostructure and the associated elemental maps of C, Ni, Ti, and O. (b) XRD patterns and (c) Raman scattering spectra of $Ti_3C_2T_X$, NiO, and $Ti_3C_2T_X$@NiO heterostructures.

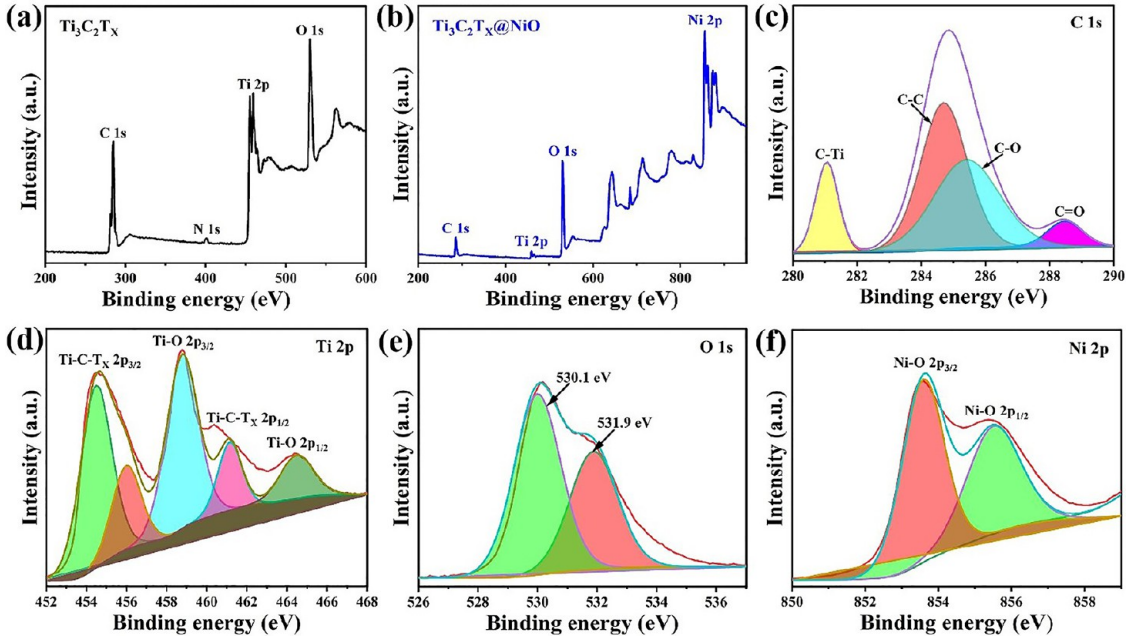

Figure 3. XPS survey spectrum of (a) $Ti_3C_2T_X$ and (b) $Ti_3C_2T_X$@NiO heterostructures. High-resolution spectra of $Ti_3C_2T_X$@NiO heterostructures: (c) C 1s, (d) Ti 2p, (e) O 1s, and (f) Ni 2p electrons.

minimize the oxidization and structural degradation of $Ti_3C_2T_X$, where ascorbic acid and the terminal functional groups of $Ti_3C_2T_X$ collectively reduced the GO, and the resulting RGO nanosheets were cross-linked into a 3D framework, into which the $Ti_3C_2T_X$@NiO heterostructure was incorporated producing a $Ti_3C_2T_X$@NiO-RGO hybrid hydrogel. From Figure 4b, one can clearly see that after hydrothermal reaction at 90 °C, the $Ti_3C_2T_X$@NiO and GO mixed colloid (mass ratio 4:1) was converted into a hydrogel with a dimension of ca. 0.8 cm in diameter and ca. 0.5 cm in height.

https://doi.org/10.1021/acsami.2c02507
ACS Appl. Mater. Interfaces 2022, 14, 19534−19546

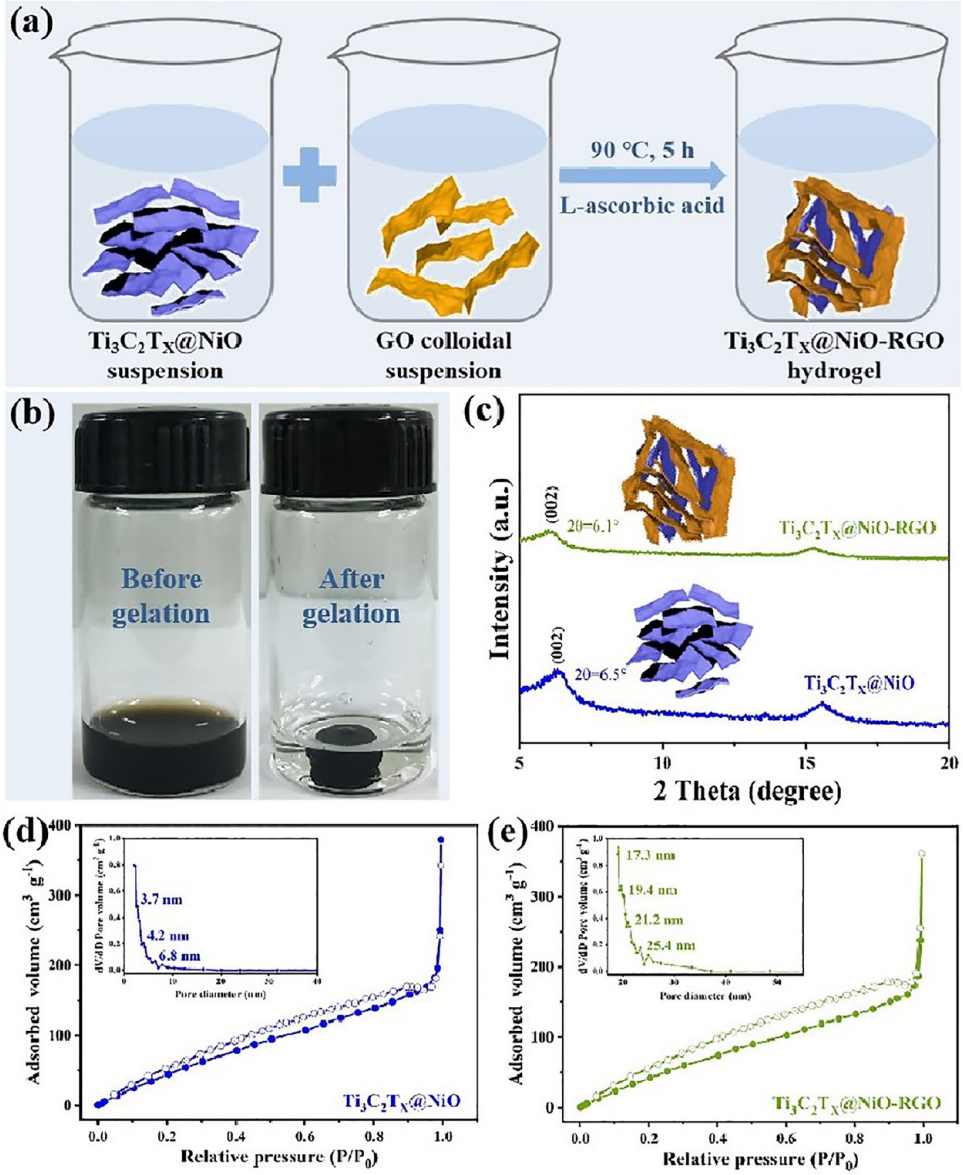

Figure 4. (a) Schematic diagram of the preparation of the $Ti_3C_2T_X$@NiO-RGO hydrogel. (b) Photograph of a $Ti_3C_2T_X$@NiO and GO colloid and the produced hydrogel. (c) XRD patterns of $Ti_3C_2T_X$@NiO and $Ti_3C_2T_X$@NiO-RGO heterostructures. Nitrogen adsorption/desorption analysis of (d) $Ti_3C_2T_X$@NiO and (e) $Ti_3C_2T_X$@NiO-RGO heterostructures. Insets are the corresponding pore size distributions.

The XRD patterns in Figure 4c show that the (002) diffraction peak shifts from $2\theta = 6.5°$ for the $Ti_3C_2T_X$@NiO powder to 6.1° for the $Ti_3C_2T_X$@NiO-RGO hydrogel after the intercalation of RGO nanosheets between $Ti_3C_2T_X$@NiO nanosheets, corresponding to an enlarged interlayer spacing from 1.32 to 1.73 nm. Additionally, one can see that the (002) peak of the hydrogel is broader than that of the powder, indicating that the restacking of $Ti_3C_2T_X$@NiO nanosheets in the assembled 3D structure was prevented, which is favorable for enhancing the rate performance and capacitance in electrochemical applications. We also characterized with HRTEM the interlayer spacings of the $Ti_3C_2T_X$@NiO-RGO hydrogel assembled with RGO nanosheets. In HRTEM measurements (Figure S1), the interlayer spacing was estimated to be 1.73 nm for the $Ti_3C_2T_X$@NiO-RGO hydrogel and 1.32 nm for $Ti_3C_2T_X$@NiO, consistent with the XRD results. The introduction of materials to expand the interlayer spacings is one of the effective strategies for preventing restacking of MXenes. Ozoemena et al. showed that introducing carbon nanospheres (CNSs)/onionlike carbons (OLCs) to an MXene compound can increase the interlayer spacings and improve the specific capacitance.[36,37]

Nitrogen adsorption/desorption measurements show that the aggregation of the $Ti_3C_2T_X$@NiO composite was effectively suppressed (Figure 4d). $Ti_3C_2T_X$@NiO features a type IV isotherm and a maximum adsorption volume at $P/P_0 = 1$, suggesting the formation of abundant micropores. In contrast, the $Ti_3C_2T_X$@NiO-RGO hydrogel features a type II isotherm and an apparent hysteresis loop at relative pressures from 0.1 to 1.0 (Figure 4e), indicative of a mesoporous structure. Notably, the $Ti_3C_2T_X$@NiO-RGO hydrogel exhibited a BET specific surface area of 331 $m^2\ g^{-1}$, over 3 times larger than that of $Ti_3C_2T_X$@NiO (86 $m^2\ g^{-1}$). In addition, the pore size distribution is investigated through the BJH method. In the inset to Figure 4d, one can see that the $Ti_3C_2T_X$@NiO powder consisted mainly of micropores

https://doi.org/10.1021/acsami.2c02507
ACS Appl. Mater. Interfaces 2022, 14, 19534−19546

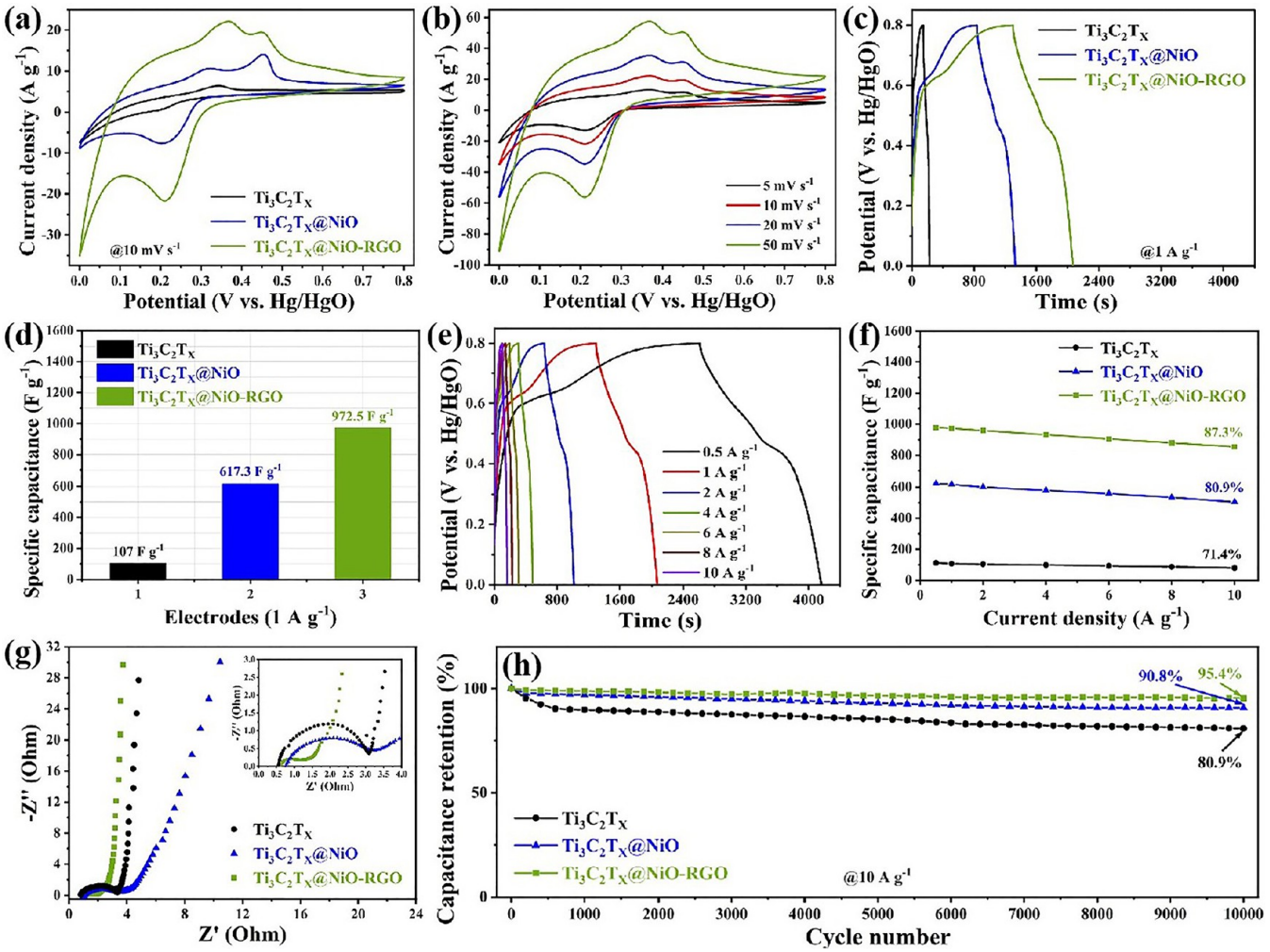

Figure 5. (a) CV curves of $Ti_3C_2T_X$, $Ti_3C_2T_X$@NiO, and $Ti_3C_2T_X$@NiO-RGO hydrogel. Potential scan rate 10 mV s^{-1}. (b) CV curves of the $Ti_3C_2T_X$@NiO-RGO hydrogel at different scan rates. (c) GCD profiles of $Ti_3C_2T_X$, $Ti_3C_2T_X$@NiO, and $Ti_3C_2T_X$@NiO-RGO hydrogel at 1 A g^{-1} and (d) the corresponding specific capacitance. (e) GCD profiles of the $Ti_3C_2T_X$@NiO-RGO hydrogel at controlled current density. (f) Specific capacitance of $Ti_3C_2T_X$, $Ti_3C_2T_X$@NiO, and $Ti_3C_2T_X$@NiO-RGO hydrogel at different current densities. (g) Nyquist plots of $Ti_3C_2T_X$, $Ti_3C_2T_X$@NiO, and $Ti_3C_2T_X$@NiO-RGO with the frequency varied from 0.01 to 10^5 Hz. The inset is the zoom-in view of the high-frequency portion. (h) Cycling stability of $Ti_3C_2T_X$, $Ti_3C_2T_X$@NiO, and $Ti_3C_2T_X$@NiO-RGO hydrogel at 10 A g^{-1} over 10,000 cycles.

featuring major pore sizes at 3.7, 4.2, and 6.8 nm, while the $Ti_3C_2T_X$@NiO-RGO hydrogel showed a larger pore size at 17.3, 19.4, 21.2, and 25.4 nm (inset to Figure 4e) in the mesoporous region. That is, the hydrogel consisted of a 3D porous interconnected structure due to $Ti_3C_2T_X$@NiO and RGO. This is conducive to reducing aggregation and enhancing the electrical conductibility of $Ti_3C_2T_X$ and hence accessibility of active surfaces for electrochemical applications.

In cyclic voltammetric (CV) assessments (Figure 5a), $Ti_3C_2T_X$, $Ti_3C_2T_X$@NiO, and $Ti_3C_2T_X$@NiO-RGO electrodes all displayed a pair of redox peaks in 1 M KOH, arising from the variation of the Ti valence state in alkaline media. In comparison with $Ti_3C_2T_X$, $Ti_3C_2T_X$@NiO and $Ti_3C_2T_X$@NiO-RGO show slightly different anodic and cathodic peaks due to reactions between Ni^{2+}/Ni^{3+} and Ti. More importantly, the $Ti_3C_2T_X$@NiO-RGO sample exhibited a far higher current density and larger integrated area, and hence a higher specific capacity, than $Ti_3C_2T_X$ and $Ti_3C_2T_X$@NiO. This demonstrates that the assembly of the 3D hydrogel structure indeed improves the pseudocapacitive performance of $Ti_3C_2T_X$@NiO-RGO. The CV profiles of the $Ti_3C_2T_X$@NiO-RGO at different sweep rates are depicted in Figure 5b. The peak positions exhibited only a slight shift with increasing sweep rate, indicating the highly reversible nature of the faradaic reactions.

To further explore the capacitive characteristics of these samples, galvanostatic charge/discharge (GCD) studies were conducted at a unified current density of 1 A g^{-1}. As shown in Figure 5c, the nonlinear GCD curves featured a clear plateau, consistent with the typical pseudocapacitive behavior and reversible and fast charge/discharge kinetics, in agreement with the CV results. Additionally, the GCD profiles show an almost symmetric triangular shape, further confirming the reversible nature of the faradic reactions. The discharge time of the $Ti_3C_2T_X$@NiO-RGO electrode was obviously longer, and the specific capacitance (972.5 F g^{-1}) was significantly greater than those of $Ti_3C_2T_X$@NiO (617.3 F g^{-1}) and $Ti_3C_2T_X$ (107 F g^{-1}) (Figure 5d). This is likely due to the gelation of $Ti_3C_2T_X$@NiO within a conductive 3D RGO interconnected hydrogel. As evidenced in Figure 5e, there is no apparent IR drop with increasing current density from 0.5 to 10 A g^{-1}, indicative of rapid transport of electrolyte ions and electrons.

https://doi.org/10.1021/acsami.2c02507
ACS Appl. Mater. Interfaces 2022, 14, 19534−19546

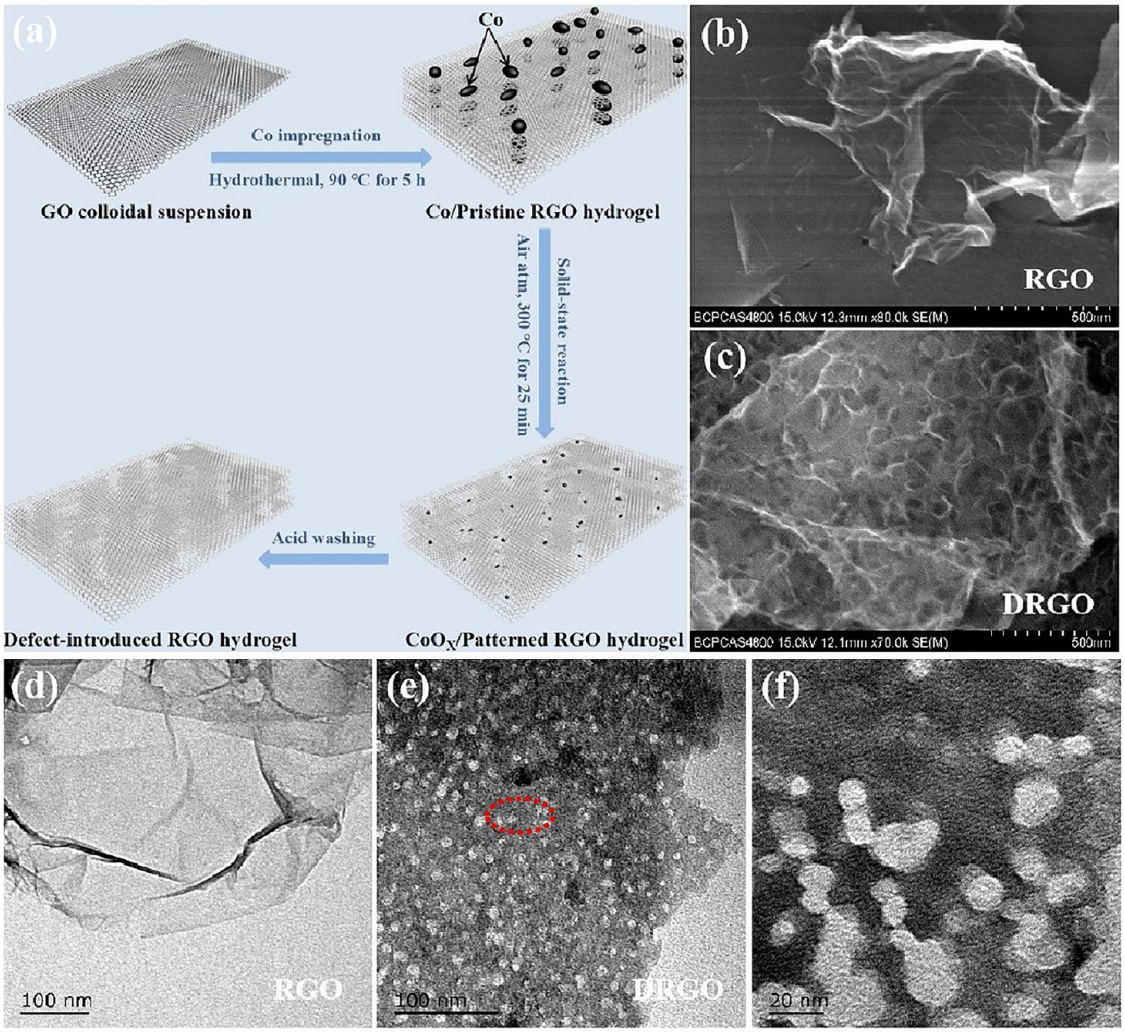

Figure 6. (a) Illustration of the preparation process of the defective RGO hydrogel. FESEM images of (b) RGO and (c) DRGO. TEM micrographs of (d) RGO and (e) DRGO. (f) Zoom-in view of the dashed region in (e).

Furthermore, the $Ti_3C_2T_X$@NiO-RGO electrode shows only a moderate decrease of the specific capacitance with current density, from 979 F g^{-1} at 0.5 A g^{-1} to 855 F g^{-1} at 10 A g^{-1} (Figure 5f). The 87.3% retention of the original specific capacitance suggests sufficient surface utilization and outstanding rate capability. As a comparison, the specific capacitance of $Ti_3C_2T_X$ and $Ti_3C_2T_X$@NiO decreases from 112 to 80 F g^{-1} (71.4% retained) and 623 to 504 F g^{-1} (80.9% retention), respectively. Notably, the specific capacitance of the $Ti_3C_2T_X$@NiO-RGO electrode was superior to those of a number of $Ti_3C_2T_X$-based electrodes reported previously (Table S1).[15,38−48] The excellent rate capability of $Ti_3C_2T_X$@NiO-RGO is attributed to the synergistic coupling interactions among the various structural constituents and the 3D interconnected framework. Specifically, the highly conductive $Ti_3C_2T_X$ core in the heterostructure provides abundant transport pathways for ions as well as active interfacial centers, whereas the ultrathin NiO shells can boost the mass transport of electrolyte ions and increase the pseudocapacitance. In addition, the wet hydrogel and the 3D architecture allow intimate contact between $Ti_3C_2T_X$@NiO and the electrolyte and quick diffusion of electrolyte ions, leading to a high-rate capability.

To investigate the conductivity behavior of these samples, electrochemical impedance measurements were conducted within the frequency range of 0.01 to 10^5 Hz. From the Nyquist plots (Figure 5g and inset), $Ti_3C_2T_X$@NiO-RGO hydrogel exhibits a lower charge-transfer resistance (R_{ct}, 3.2 Ω) than $Ti_3C_2T_X$@NiO (5.6 Ω), indicating faster electron transfer kinetics. Furthermore, the device series resistance (R_s) was ca. 4.3 Ω for $Ti_3C_2T_X$@NiO and 2.1 Ω for $Ti_3C_2T_X$@NiO-RGO, suggesting that gelation of the $Ti_3C_2T_X$@NiO heterostructure indeed increased the electrical conductivity of the composite. In addition, the slope of the linear segment for $Ti_3C_2T_X$@NiO-RGO is greater compared with that of $Ti_3C_2T_X$@NiO, indicating increasingly capacitive behavior of the former.

Long-cycle lifetime is vital to practical applications, which was evaluated via GCD measurements at 10 A g^{-1} for 10,000 cycles, as shown in Figure 5h. About 95.4% retention of its initial capacitance (80.9% of $Ti_3C_2T_X$ and 90.8% of $Ti_3C_2T_X$@NiO) was observed, and the GCD profiles did not vary obviously in shape, indicating a small leakage current and good cycling performance of the $Ti_3C_2T_X$@NiO-RGO hydrogel.

3.2. DRGO Cathode. Owing to the high electrical conductibility, abundant mesoporous construction, and large specific surface area, defective graphene has emerged as a promising cathode material for ASCs. Herein, a DRGO

https://doi.org/10.1021/acsami.2c02507
ACS Appl. Mater. Interfaces 2022, 14, 19534−19546

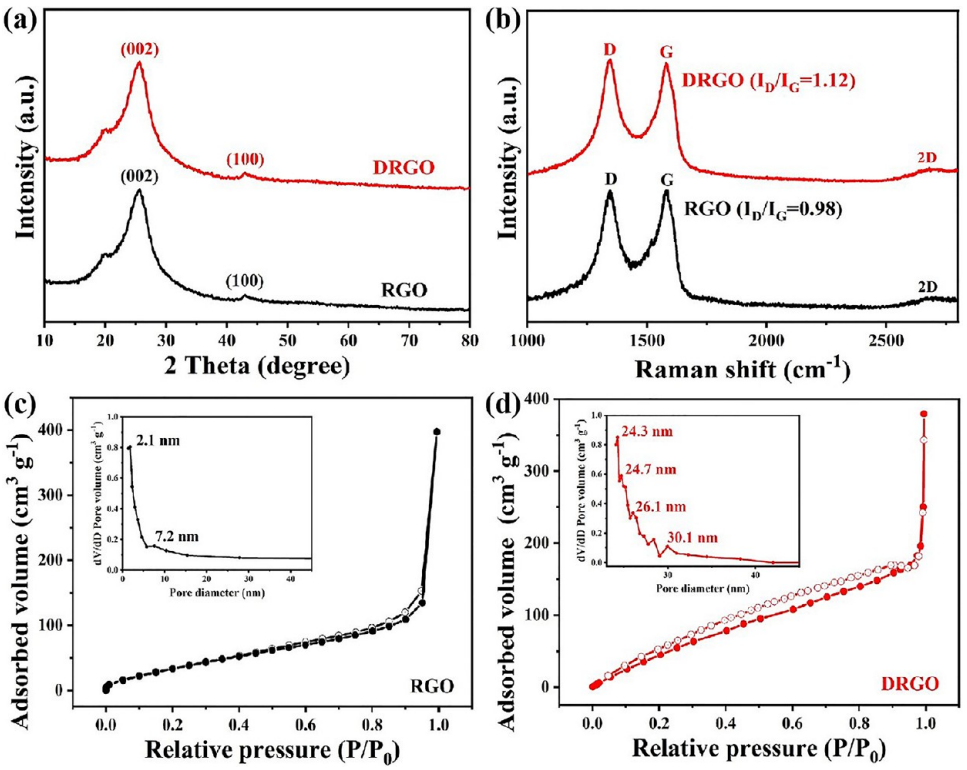

Figure 7. (a) XRD patterns and (b) Raman scattering spectra of RGO and DRGO. Nitrogen adsorption/desorption isotherms of (c) RGO and (d) DRGO. Insets are the associated pore size distributions.

hydrogel was prepared by a multistep strategy as outlined in Figure 6a. In FESEM tests, RGO nanosheets can be seen to exhibit a wrinkled morphology (Figure 6b), whereas DRGO shows well-defined mesoporous characteristics (Figure 6c). The average pore size of DRGO is around 25 nm, and the pore distribution is rather uniform. The morphology was further analyzed by TEM measurements, where the samples showed a wrinkled, curled paper-like structure. Before the patterning process (Figure 6d), the exterior walls of RGO were cavity-free with an ordered graphitic structure; yet, after the Co-catalyzed gasification and acid digestion treatment, plentiful mesopores were produced, as shown in Figure 6e,f.

The structural variations were also analyzed by XRD and Raman spectroscopic measurements. In the diffraction patterns in Figure 7a, the peaks at 2θ = ca. 26 and 43° are due to the graphitic carbon (002) and (100) crystalline planes, respectively. Figure 7b shows the corresponding Raman spectra, where the G band appears at ca. 1587 cm^{-1} and the D band appears at ca. 1352 cm^{-1}.[49] Additionally, the D and G band intensity ratio is somewhat greater for DRGO (I_D/I_G = 1.12) than for RGO (I_D/I_G = 0.98), confirming a more defective structure of the former, where the structural defects likely arose from the Co-catalyzed cavity production.[50]

Figure 7c,d depicts the corresponding nitrogen adsorption/desorption isotherms. Pristine RGO (Figure 7c) can be seen to possess a type II isotherm and shows the maximum adsorption at P/P_0 = 1, suggestive of abundant micropores in the sample. For comparison, DRGO shows a type IV isotherm and an apparent hysteresis loop within the relative pressure range of 0.1−1.0, which is attributed to the formation of a mesoporous characteristic. From the inset to Figure 7c, pristine RGO can be seen to display a wide range of pore sizes, with the major pore sizes at 2.1 and 7.2 nm, indicating that the sample consisted mainly of micropores. For DRGO, the main pore sizes are 24.3, 24.7, 26.1, and 30.1 nm, consistent with the mesoporous structure (inset to Figure 7d). The BET specific surface area of DRGO is estimated to be 591 m^2 g^{-1}, markedly greater than that (198 m^2 g^{-1}) of pristine RGO.

The TGA curves are shown in Figure 8a. One can see that the Co/RGO mixture shows a faster weight loss at a lower temperature of ca. 400 °C than pristine RGO and DRGO. This can be ascribed to cobalt oxide that facilitated the oxidation of carbon, as lattice oxygen can promote the formation of C−O bonds and release of CO gas, and hence the formation of pores in the graphene scaffolds.[50] The porosity is further enhanced by acid leaching to remove the Co particles.

The electrochemical property of these samples was then examined within the potential range of 0 to −1.0 V in a 1 M KOH electrolyte. Figure 8b displays the CV curves of RGO and DRGO hydrogels at the potential sweep rate of 10 mV s^{-1}, which are all quasi-rectangular in shape. The DRGO electrode possesses a greater integrated charge area than the RGO counterpart, suggestive of a larger specific capacitance and quicker charge/discharge capability for power storage. Figure 8c shows the CV profiles of the DRGO hydrogel at various scan rates. Obviously, with increasing scanning rates, the CV curve shape remains virtually invariant, indicative of a high rate stability and low series resistance.

The capacitive performance was further evaluated by GCD measurements at the same current density of 1 A g^{-1}. From Figure 8d, the DRGO hydrogel electrode can be observed to display a drastically greater specific capacitance (259 F g^{-1}) than RGO (174 F g^{-1}), revealing an improved charge storage performance with the introduction of defects via a Co-catalyzed gasification process, in agreement with the CV results. From Figure 8e, there is no obvious IR drop in the

https://doi.org/10.1021/acsami.2c02507
ACS Appl. Mater. Interfaces 2022, 14, 19534−19546

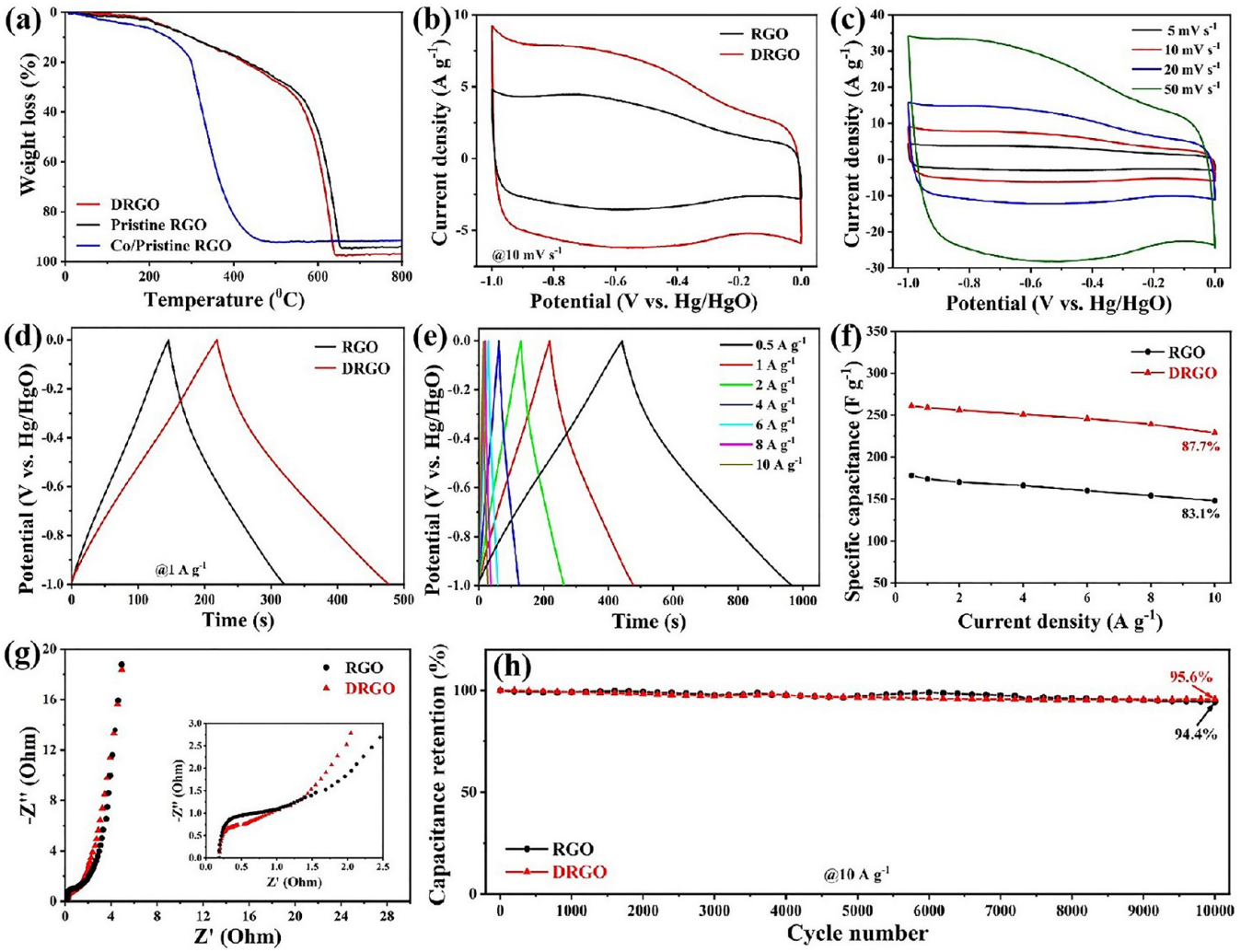

Figure 8. (a) TGA of the Co/pristine RGO mixture, pristine RGO, and DRGO. Electrochemical performance of RGO and DRGO: (b) CV curves of RGO and DRGO at the potential scan rate of 10 mV s^{-1}. (c) CV curves of DRGO at various scan rates. (d) GCD curves of RGO and DRGO at the current density of 1 A g^{-1}. (e) GCD curves of DRGO at various current densities. (f) Specific capacitance vs current density plot of RGO and DRGO. (g) Nyquist impedance plots of RGO and DRGO. The inset is the zoom-in view of the high-frequency part. (h) Cycling stability of RGO and DRGO at 10 A g^{-1} for 10,000 cycles.

GCD profiles of the DRGO hydrogel at current densities from 0.5 to 10 A g^{-1}, indicative of good capacitive behavior and minimal internal resistance. Additionally, the GCD curves remained largely symmetrical, indicating an excellent rate capability. Taken together, these CV and GCD results imply highly reversible EDLC behaviors of the DRGO hydrogel electrode. Figure 8f depicts the variation of specific capacitances with current density of the RGO and DRGO hydrogel electrodes. The DRGO electrode features a high specific capacitance, 259 F g^{-1} at 1 A g^{-1} and 229 F g^{-1} at 10 A g^{-1} (87.7% retention), compared to 174 and 148 F g^{-1} for RGO (83.1% retention). This suggests better rate stability of the DRGO hydrogel electrode most likely due to a small charge-transfer resistance.

Note that the electrical conductivity of the DRGO hydrogel was retained despite the formation of the defect structure. From the Nyquist plots in Figure 8g and inset, it can be observed that the R_{ct} of DRGO hydrogel (2.3 Ω) is similar to that of the RGO hydrogel (2.2 Ω), whereas the slope of the linear segment is greater for the DRGO electrode compared to that of RGO, consistent with the better capacitive performance of the DRGO hydrogel. Moreover, this implies that gasification occurred only at the carbon interacting with metal oxide particles, whereas the planar sheets and excellent conductivity of graphitic carbon were retained. The cycling performance of the RGO and DRGO hydrogel electrodes was then examined via a repeated GCD process at 10 A g^{-1} current density (Figure 8h). The DRGO hydrogel still retains 95.6% of the initial capacity after 10,000 cycles, while only about 94.4% for the RGO hydrogel, indicating a much better stability of the DRGO hydrogel electrode.

Notably, this 3D DRGO hydrogel electrode outperformed a number of relevant carbon-based composites for SCs reported previously (Table S2).[51−63] The electrochemical performance can be ascribed to the abundant mesoporosity, excellent electrical conductivity, and high rate stability.

3.3. $Ti_3C_2T_X$@NiO-RGO//DRGO ASC. Because of the excellent electrode performances, $Ti_3C_2T_X$@NiO-RGO and DRGO were then utilized as the cathode and anode, respectively, in the construction of an ASC (Figure 9a) with 1 KOH as the electrolyte and a porous polymer membrane separator. The anode-to-cathode mass ratio was optimized at

https://doi.org/10.1021/acsami.2c02507
ACS Appl. Mater. Interfaces 2022, 14, 19534−19546

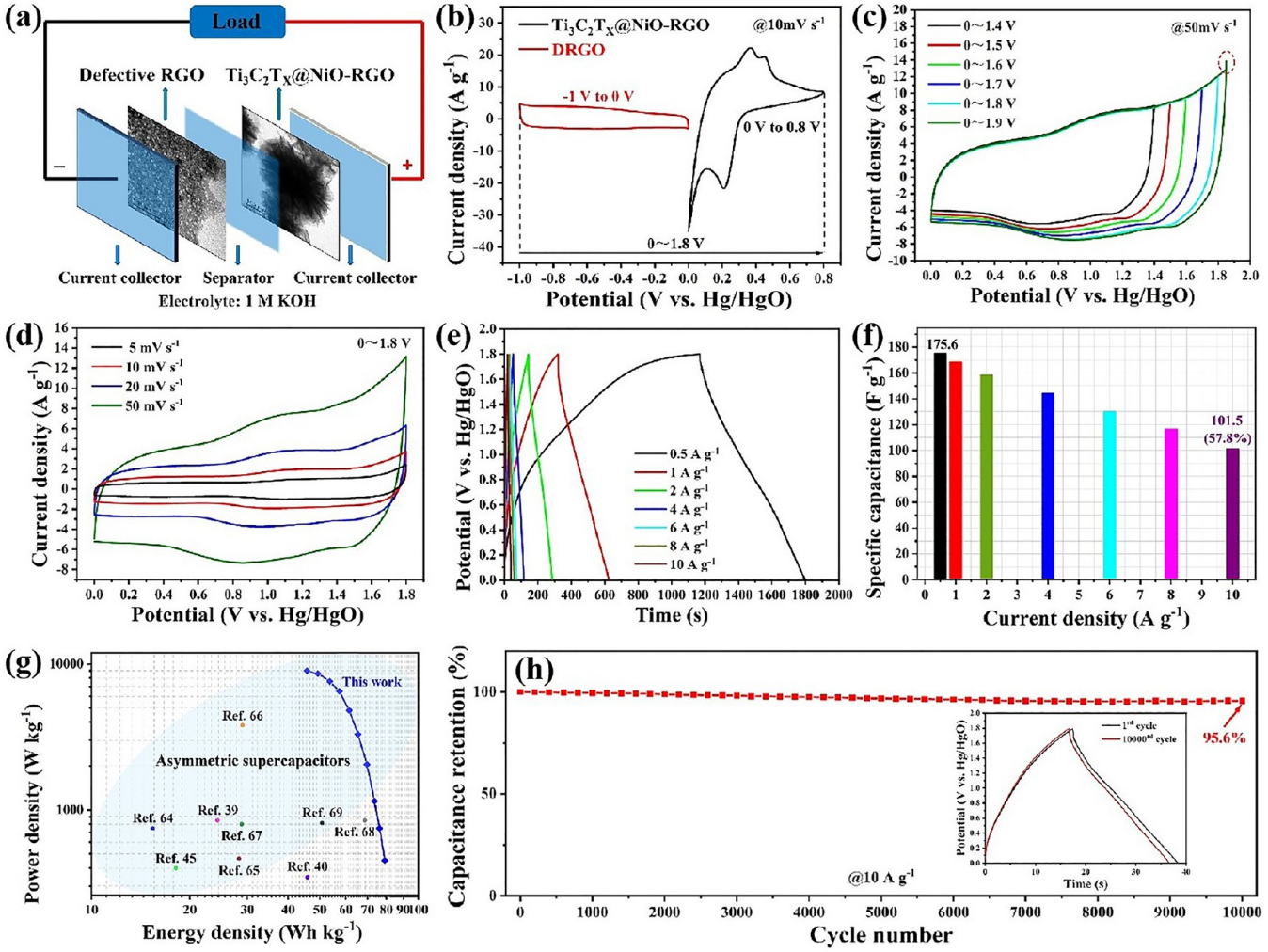

Figure 9. Capacitive performance of the $Ti_3C_2T_X$@NiO-RGO//DRGO ASC device: (a) Schematic for the assembly of the ASC. (b) CV curves of individual $Ti_3C_2T_X$@NiO-RGO anode and DRGO cathode at a scan rate of 10 mV s^{-1}. (c) CV curves of the ASC device at 10 mV s^{-1} with various potential voltages. (d) CV curves of the ASC device at various scan rates between 0 and 1.8 V. (e) GCD curves of the ASC device at different current densities between 0 and 1.8 V. (f) Specific capacitances estimated from the GCD data at various current densities. (g) Ragone plot of the present ASC device in comparison to relevant $Ti_3C_2T_X$-based ASCs reported in the literature. (h) Cycling performance of the ASC device at 10 A g^{-1}, with the inset showing the 1st and 10,000th GCD curves during the cycling measurements.

approximately 1:3 (total active materials 4 mg), according to charge balance theory.[35]

As displayed in Figure 9b, the CV curves were first acquired at 10 mV s^{-1} and displayed a 0 to 0.8 V potential window for $Ti_3C_2T_X$@NiO-RGO and from -1 to 0 V for DRGO electrodes, which determine the potential range of the ASC. Figure 9c shows the CV profiles of the ASC at 50 mV within different voltage windows (0−1.4, 0−1.5, 0−1.6, 0−1.7, 0−1.8, and 0−1.9 V) s^{-1}. Notably, the voltage window can be enlarged to 1.8 V. A clear sharp-peak current enhancement in the red circle was discovered due to marked oxygen evolution with the voltage range further increased to 1.9 V. To maximize the cycle life, the ASC operating voltage was set at 1.8 V. The typical CV curves of the $Ti_3C_2T_X$@NiO-RGO//DRGO ASC at different scan rates are depicted in Figure 9d, where a pair of clearly defined redox peaks emerge due to the pseudocapacitive behavior of the reversible redox processes between Ni^{2+}/Ni^{3+} and Ti, indicating that faradic reaction is the dominant charge storage mechanism within this voltage window. Additionally, the CV curves remained almost unchanged in shape with increasing sweep rate, suggesting an excellent rate capability and capacitive behavior of the ASC.

This pseudocapacitive nature of the electrode materials is also manifested in the GCD curves (Figure 9e), which display a curvature at similar voltages. Moreover, the symmetric triangular shape with no clear IR drop of the GCD curves once again confirms the excellent capacity and reversible operation of the device. The ASC specific capacitance (C) was then evaluated from the GCD curves at varied current densities: 175.6 at 0.5 A g^{-1} and 101.5 F g^{-1} at 10 A g^{-1} (Figure 9f). This remarkable performance (57.8% of its initial value) can be attributable to matched capacity and balanced fast redox kinetics. Additionally, at a power density of 450 W kg^{-1}, the ASC displayed an ultrahigh energy density of 79.02 W h $kg^{-1}$and retained 45.68 Wh kg^{-1} at a significantly higher power density of 9000 W kg^{-1}. This performance is better than those of nickel- and $Ti_3C_2T_X$-based ASCs reported previously, as evidenced in the Ragone plot (Figure 9g).[39,40,45,64−69] Repeated GCD measurements were then carried out at 10 A g^{-1} over 10,000 cycles to probe the cycling stability. From Figure 9h, this ASC device can be seen to retain 95.6% of its

https://doi.org/10.1021/acsami.2c02507
ACS Appl. Mater. Interfaces 2022, 14, 19534−19546

starting capacitance, with virtually no change of the GCD curves (inset to Figure 9h), indicating remarkable cycling stability.

4. CONCLUSIONS

In summary, a 3D layered $Ti_3C_2T_X$@NiO-RGO heterostructured hydrogel was prepared through a facile two-step strategy. NiO nanoflowers were evenly deposited onto the surface of highly conductive $Ti_3C_2T_X$ forming a close-contact framework, which facilitated mass transport of electrolyte ions during charge and discharge. In addition, the 3D interconnected structure significantly reduced the agglomeration of $Ti_3C_2T_X$@NiO, resulting in a remarkable specific capacitance of 979 F g^{-1} at 0.5 A g^{-1} and an outstanding rate capability (87.3% at 10 A g^{-1}). In addition, a 3D porous DRGO hydrogel was produced by a low-cost hydrothermal method, followed by cobalt-catalyzed gasification. With the formation of abundant mesopores, the DRGO hydrogel possessed a specific capacitance as high as 261 F g^{-1} at 0.5 A g^{-1}. The $Ti_3C_2T_X$@NiO-RGO and DRGO hydrogels were then exploited as free-standing anode and cathode for the assembly of an ASC device, which featured a 1.8 V expanded voltage window, a 79.02 Wh kg^{-1} maximum energy density at a power density of 450 W kg^{-1} and 45.68 Wh kg^{-1} at 9000 W kg^{-1}, and retention up to 95.6% of the capacitance after 10,000 cycles at 10 A g^{-1}. These results offer an efficient strategy to the design and engineering of MXene-based heterostructured hydrogels as high-energy-density ASC electrodes.

■ ASSOCIATED CONTENT

Supporting Information

The Supporting Information is available free of charge at https://pubs.acs.org/doi/10.1021/acsami.2c02507.

Performances of relevant electrodes and SCs (PDF)

■ AUTHOR INFORMATION

Corresponding Authors

Zenghui Qiu − *College of Mathematics & Physics, Beijing University of Chemical Technology, Beijing 100029, China; Beijing Bioprocess Key Laboratory, Beijing University of Chemical Technology, Beijing 100029, China*; Email: zhqiu@buct.edu.cn

Haijun Xu − *College of Mathematics & Physics, Beijing University of Chemical Technology, Beijing 100029, China; Beijing Bioprocess Key Laboratory, Beijing University of Chemical Technology, Beijing 100029, China*; Email: hjxu@buct.edu.cn

Shaowei Chen − *Department of Chemistry and Biochemistry, University of California, Santa Cruz, California 95064, United States*; orcid.org/0000-0002-3668-8551; Email: shaowei@ucsc.edu

Authors

Weiwen Chen − *College of Mathematics & Physics, Beijing University of Chemical Technology, Beijing 100029, China; Beijing Bioprocess Key Laboratory, Beijing University of Chemical Technology, Beijing 100029, China*

Chunfeng Hao − *College of Mathematics & Physics, Beijing University of Chemical Technology, Beijing 100029, China; Beijing Bioprocess Key Laboratory, Beijing University of Chemical Technology, Beijing 100029, China*

Xin Zhang − *College of Mathematics & Physics, Beijing University of Chemical Technology, Beijing 100029, China; Beijing Bioprocess Key Laboratory, Beijing University of Chemical Technology, Beijing 100029, China*

Bingzhe Yu − *Department of Chemistry and Biochemistry, University of California, Santa Cruz, California 95064, United States*

Complete contact information is available at: https://pubs.acs.org/10.1021/acsami.2c02507

Author Contributions

The manuscript was written through contributions of all authors. All authors have given approval to the final version of the manuscript.

Notes

The authors declare no competing financial interest.

■ ACKNOWLEDGMENTS

This work was supported by the National Natural Science Foundation of China (21676015, 52073022, and 31961133017) and the National Basic Research Program of China (52014CB745100). S.W.C. thanks the National Science Foundation (CHE-1900235) for partial support of the work.

■ REFERENCES

(1) Ozoemena, K. I.; Chen, S. Nanomaterials in Advanced Batteries and Supercapacitors. In *Nanostructure Science and Technology*, 1st ed.; Springer International Publishing: Imprint: Springer: Cham, 2016.

(2) Ran, F.; Chen, S. *Advanced Nanomaterials for Electrochemical Energy Conversion and Storage*, 1st ed.; Elsevier: Walthom, 2019.

(3) Chatterjee, D. P.; Nandi, A. K. A review on the Recent Advances in Hybrid Supercapacitors. *J. Mater. Chem. A.* **2021**, *9*, 15880−15918.

(4) Reece, R.; Lekakou, C.; Smith, P. A. A High-Performance Structural Supercapacitor. *ACS Appl. Mater. Interfaces* **2020**, *12*, 25683−25692.

(5) Qin, H.; Liu, P.; Chen, C.; Cong, H. P.; Yu, S. H. A Multi-responsive Healable Supercapacitor. *Nat. Commun.* **2021**, *12*, No. 4297.

(6) Ma, H.; Chen, H.; Hu, Y.; Yang, B.; Feng, J.; Xu, Y.; Sun, Y.; Cheng, H.; Li, C.; Yan, X.; Qu, L. Aqueous Rocking-chair Aluminum-ion Capacitors Enabled by a Self-adaptive Electrochemical Pore-Structure Remolding Approach. *Energy Environ. Sci.* **2022**, *15*, 1131−1143.

(7) Banda, H.; Dou, J. H.; Chen, T.; Libretto, N. J.; Chaudhary, M.; Bernard, G. M.; Miller, J. T.; Michaelis, V. K.; Dinca, M. High-Capacitance Pseudocapacitors from Li(+) Ion Intercalation in Nonporous, Electrically Conductive 2D Coordination Polymers. *J. Am. Chem. Soc.* **2021**, *143*, 2285−2292.

(8) Naguib, M.; Kurtoglu, M.; Presser, V.; Lu, J.; Niu, J.; Heon, M.; Hultman, L.; Gogotsi, Y.; Barsoum, M. W. Two-dimensional Nanocrystals Produced by Exfoliation of Ti_3AlC_2. *Adv. Mater.* **2011**, *23*, 4248−4253.

(9) Lukatskaya, M. R.; Kota, S.; Lin, Z.; Zhao, M.-Q.; Shpigel, N.; Levi, M. D.; Halim, J.; Taberna, P.-L.; Barsoum, M. W.; Simon, P.; Gogotsi, Y. Ultra-high-rate Pseudocapacitive Energy Storage in Two-dimensional Transition Metal Carbides. *Nat. Energy* **2017**, *2*, No. 17105.

(10) Gogotsi, Y.; Anasori, B. The Rise of MXenes. *ACS Nano* **2019**, *13*, 8491−8494.

(11) Alhabeb, M.; Maleski, K.; Anasori, B.; Lelyukh, P.; Clark, L.; Sin, S.; Gogotsi, Y. Guidelines for Synthesis and Processing of Two-Dimensional Titanium Carbide ($Ti_3C_2T_X$ MXene). *Chem. Mater.* **2017**, *29*, 7633−7644.

(12) Lukatskaya, M. R.; Mashtalir, O.; Ren, C. E.; Dall'Agnese, Y.; Rozier, P.; Taberna, P. L.; Naguib, M.; Simon, P.; Barsoum, M. W.;

Gogotsi, Y. Cation Intercalation and High Volumetric Capacitance of Two-dimensional Titanium Carbide. *Science* **2013**, *341*, 1502−1505.
(13) Ghidiu, M.; Lukatskaya, M. R.; Zhao, M. Q.; Gogotsi, Y.; Barsoum, M. W. Conductive Two-dimensional Titanium Carbide 'Clay' with High Volumetric Capacitance. *Nature* **2014**, *516*, 78−81.
(14) Huang, H.; Cui, J.; Liu, G.; Bi, R.; Zhang, L. Carbon-Coated MoSe2/MXene Hybrid Nanosheets for Superior Potassium Storage. *ACS Nano* **2019**, *13*, 3448−3456.
(15) Song, J.; Hu, P.; Liu, Y.; Song, W.; Wu, X. Enhanced Electrochemical Performance of $Co_2NiO_4/Ti_3C_2T_X$ Structures through Coupled Synergistic Effects. *ChemistrySelect* **2019**, *4*, 12886−12890.
(16) Navarro-Suárez, A. M.; Van Aken, K. L.; Mathis, T.; Makaryan, T.; Yan, J.; Carretero-González, J.; Rojo, T.; Gogotsi, Y. Development of Asymmetric Supercapacitors with Titanium Carbide-reduced Graphene Oxide Couples as Electrodes. *Electrochim. Acta* **2018**, *259*, 752−761.
(17) Zhu, M.; Huang, Y.; Deng, Q.; Zhou, J.; Pei, Z.; Xue, Q.; Huang, Y.; Wang, Z.; Li, H.; Huang, Q.; Zhi, C. Highly Flexible, Freestanding Supercapacitor Electrode with Enhanced Performance Obtained by Hybridizing Polypyrrole Chains with MXene. *Adv. Energy Mater.* **2016**, *6*, No. 1600969.
(18) Shao, W.; Tebyetekerwa, M.; Marriam, I.; Li, W.; Wu, Y.; Peng, S.; Ramakrishna, S.; Yang, S.; Zhu, M. Polyester@MXene Nanofibers-based Yarn Electrodes. *J. Power Sources* **2018**, *396*, 683−690.
(19) Naguib, M.; Mashtalir, O.; Lukatskaya, M. R.; Dyatkin, B.; Zhang, C.; Presser, V.; Gogotsi, Y.; Barsoum, M. W. One-step Synthesis of Nanocrystalline Transition Metal Oxides on Thin Sheets of Disordered Graphitic Carbon by Oxidation of MXenes. *Chem. Commun.* **2014**, *50*, 7420−7423.
(20) Yang, Z.; Xu, F.; Zhang, W.; Mei, Z.; Pei, B.; Zhu, X. Controllable Preparation of Multishelled NiO Hollow Nanospheres via Layer-by-layer Self-assembly for Supercapacitor Application. *J. Power Sources* **2014**, *246*, 24−31.
(21) Zhao, M. Q.; Xie, X.; Ren, C. E.; Makaryan, T.; Anasori, B.; Wang, G.; Gogotsi, Y. Hollow MXene Spheres and 3D Macroporous MXene Frameworks for Na-Ion Storage. *Adv. Mater.* **2017**, *29*, No. 1702410.
(22) Ma, Y.; Yue, Y.; Zhang, H.; Cheng, F.; Zhao, W.; Rao, J.; Luo, S.; Wang, J.; Jiang, X.; Liu, Z.; et al. 3D Synergistical MXene/Reduced Graphene Oxide Aerogel for a Piezoresistive Sensor. *ACS Nano* **2018**, *12*, 3209−3216.
(23) Zhang, Y. Z.; El-Demellawi, J. K.; Jiang, Q.; Ge, G.; Liang, H.; Lee, K.; Dong, X.; Alshareef, H. N. MXene Hydrogels: Fundamentals and Applications. *Chem. Soc. Rev.* **2020**, *49*, 7229−7251.
(24) Hu, H.; Zhao, Z.; Wan, W.; Gogotsi, Y.; Qiu, J. Ultralight and Highly Compressible Graphene Aerogels. *Adv. Mater.* **2013**, *25*, 2219−2223.
(25) Zhang, L.; Shi, G. Preparation of Highly Conductive Graphene Hydrogels for Fabricating Supercapacitors with High Rate Capability. *J. Phys. Chem. C* **2011**, *115*, 17206−17212.
(26) Stoller, M. D.; Ruoff, R. S. Best Practice Methods for Determining an Electrode Material's Performance for Ultracapacitors. *Energy Environ. Sci.* **2010**, *3*, 1294−1301.
(27) Rao, C. N.; Sood, A. K.; Subrahmanyam, K. S.; Govindaraj, A. Graphene: the New Two-dimensional Nanomaterial. *Angew. Chem. Int. Ed.* **2009**, *48*, 7752−7777.
(28) Liu, B.; Shioyama, H.; Jiang, H.; Zhang, X.; Xu, Q. Metal-Organic Framework (MOF) as a Template for Syntheses of Nanoporous Carbons as Electrode Materials for Supercapacitor. *Carbon* **2010**, *48*, 456−463.
(29) Torad, N. L.; Hu, M.; Kamachi, Y.; Takai, K.; Imura, M.; Naito, M.; Yamauchi, Y. Facile Synthesis of Nanoporous Carbons with Controlled Particle Sizes by Direct Carbonization of Monodispersed ZIF-8 Crystals. *Chem. Commun.* **2013**, *49*, 2521−2523.
(30) Chen, Z.; Lin, Y.-M.; Rooks, M. J.; Avouris, P. Graphene Nano-ribbon Electronics. *Phys. E* **2007**, *40*, 228−232.
(31) Pang, S.; Tsao, H. N.; Feng, X.; Müllen, K. Patterned Graphene Electrodes from Solution-Processed Graphite Oxide Films for Organic Field-Effect Transistors. *Adv. Mater.* **2009**, *21*, 3488−3491.
(32) Bai, H.; Li, C.; Wang, X.; Shi, G. On the Gelation of Graphene Oxide. *J. Phys. Chem. C* **2011**, *115*, 5545−5551.
(33) Pei, S.; Cheng, H.-M. The Reduction of Graphene Oxide. *Carbon* **2012**, *50*, 3210−3228.
(34) Stankovich, S.; Dikin, D. A.; Dommett, G. H.; Kohlhaas, K. M.; Zimney, E. J.; Stach, E. A.; Piner, R. D.; Nguyen, S. T.; Ruoff, R. S. Graphene-based Composite Materials. *Nature* **2006**, *442*, 282−286.
(35) Devan, R. S.; Patil, R. A.; Lin, J.-H.; Ma, Y.-R. One-Dimensional Metal-Oxide Nanostructures: Recent Developments in Synthesis, Characterization, and Applications. *Adv. Funct. Mater.* **2012**, *22*, 3326−3370.
(36) Melchior, S. A.; Raju, K.; Ike, I. S.; Erasmus, R. M.; Kabongo, G.; Sigalas, I.; Iyuke, S. E.; Ozoemena, K. I. High-Voltage Symmetric Supercapacitor Based on 2D Titanium Carbide (MXene, Ti_2CT_X)/Carbon Nanosphere Composites in a Neutral Aqueous Electrolyte. *J. Eletrochem.Soc.* **2018**, *165*, A501−A511.
(37) Habib, I.; Ferrer, P.; Ray, S. C.; Ozoemena, K. I. Interrogating the Impact of Onion-like Carbons on the Supercapacitive Properties of MXene (Ti_2CT_X). *J. Appl. Phys.* **2019**, *126*, No. 134301.
(38) Wang, X.; Li, H.; Li, H.; Lin, S.; Ding, W.; Zhu, X.; Sheng, Z.; Wang, H.; Zhu, X.; Sun, Y. 2D/2D 1T-MoS_2/Ti_3C_2 MXene Heterostructure with Excellent Supercapacitor Performance. *Adv. Funct. Mater.* **2020**, *30*, No. 0190302.
(39) Chen, X.; Liu, Y.; Zhou, Q.; Su, F. Facile Synthesis of $MnO_2/Ti_3C_2T_X$/CC as Positive Electrode of All-Solid-State Flexible Asymmetric Supercapacitor. *ChemistrySelect* **2020**, *5*, 14768−14775.
(40) Zhao, R.; Wang, M.; Zhao, D.; Li, H.; Wang, C.; Yin, L. Molecular-Level Heterostructures Assembled from Titanium Carbide MXene and Ni-Co-Al Layered Double-Hydroxide Nanosheets for All-Solid-State Flexible Asymmetric High-Energy Supercapacitors. *ACS Energy Lett.* **2018**, *3*, 132−140.
(41) Chen, W.; Zhang, D.; Yang, K.; Luo, M.; Yang, P.; Zhou, X. Mxene ($Ti_3C_2T_X$)/cellulose Nanofiber/Porous Carbon Film as Free-Standing Electrode for Ultrathin and Flexible Supercapacitors. *Chem. Eng. J.* **2021**, *413*, No. 127524.
(42) Wu, W.; Niu, D.; Zhu, J.; Gao, Y.; Wei, D.; Zhao, C.; Wang, C.; Wang, F.; Wang, L.; Yang, L. Hierarchical Architecture of Ti_3C_2@PDA/$NiCo_2S_4$ Composite Electrode as High-performance Supercapacitors. *Ceram. Int.* **2019**, *45*, 16261−16269.
(43) Zhao, Y.; Guo, J.; Liu, A.; Ma, T. 2D Heterostructure Comprised of Ni_3S_2/d-Ti_3C_2 Supported on Ni Foam as Binder-free Electrode for Hybrid Supercapacitor. *J. Alloys Compd.* **2020**, *814*, No. 152271.
(44) Chen, J.; Ren, Y.; Zhang, H.; Qi, J.; Sui, Y.; Wei, F. Ni-Co-Fe Layered Double Hydroxide Coated on Ti_3C_2 MXene for High-Performance Asymmetric Supercapacitor. *Appl. Surf. Sci.* **2021**, *562*, No. 150116.
(45) Guo, J.; Zhao, Y.; liu, A.; Ma, T. Electrostatic Self-assembly of 2D Delaminated MXene (Ti_3C_2) onto Ni Foam with Superior Electrochemical Performance for Supercapacitor. *Electrochim. Acta* **2019**, *305*, 164−174.
(46) Wei, D.; Wu, W.; Zhu, J.; Wang, C.; Zhao, C.; Wang, L. A facile Strategy of Polypyrrole Nanospheres Grown on Ti_3C_2-MXene Nanosheets as Advanced Supercapacitor Electrodes. *J. Electroanal. Chem.* **2020**, *877*, No. 114538.
(47) Pan, Z.; Ji, X. Facile synthesis of nitrogen and oxygen co-doped C@Ti_3C_2 MXene for high performance symmetric supercapacitors. *J. Power Sources* **2019**, *439*, No. 227068.
(48) Liu, C.; Bai, Y.; Li, W.; Yang, F.; Zhang, G.; Pang, H. In Situ Growth of Three-Dimensional MXene/Metal-Organic Framework Composites for High-Performance Supercapacitors. *Angew. Chem. Int. Ed.* **2022**, *61*, No. e202116282.
(49) Ferrari, A. C.; Meyer, J. C.; Scardaci, V.; Casiraghi, C.; Lazzeri, M.; Mauri, F.; Piscanec, S.; Jiang, D.; Novoselov, K. S.; Roth, S.; Geim, A. K. Raman Spectrum of Graphene and Graphene Layers. *Phys. Rev. Lett.* **2006**, *97*, No. 187401.

https://doi.org/10.1021/acsami.2c02507
ACS Appl. Mater. Interfaces 2022, 14, 19534−19546

(50) Wang, H.-W.; Hu, Z.-A.; Chang, Y.-Q.; Chen, Y.-L.; Wu, H.-Y.; Zhang, Z.-Y.; Yang, Y.-Y. Design and Synthesis of $NiCo_2O_4$-reduced Graphene Oxide Composites for High Performance Supercapacitors. *J. Mater. Chem.* **2011**, *21*, 10504−10511.
(51) Wen, P.; Gong, P.; Mi, Y.; Wang, J.; Yang, S. Scalable Fabrication of High Quality Graphene by Exfoliation of Edge Sulfonated Graphite for Supercapacitor Application. *RSC Adv.* **2014**, *4*, 35914−35918.
(52) Benedetti, M.; Girelli, C. R.; Antonucci, D.; De Pascali, S. A.; Fanizzi, F. P. New method for the synthesis of [PtCl{η1-$CH_2C(O)$-R}(N-N)] ketonyl derivatives starting from the Zeise's salt. *Inorg. Chim. Acta* **2014**, *413*, 109−114.
(53) Zhu, T.; Zhou, J.; Li, Z.; Li, S.; Si, W.; Zhuo, S. Hierarchical Porous and N-doped Carbon Nanotubes Derived from Polyaniline for Electrode Materials in Supercapacitors. *J. Mater. Chem. A* **2014**, *2*, 12545−12551.
(54) El-Kady, M. F.; Strong, V.; Dubin, S.; Kaner, R. B. Laser Scribing of High-performance and Flexible Graphene-based Electrochemical Capacitors. *Science* **2012**, *335*, 1326−1330.
(55) Shang, T.-X.; Zhang, M.-Y.; Jin, X.-J. Easy procedure to prepare nitrogen-containing activated carbons for supercapacitors. *RSC Adv.* **2014**, *4*, 39037−39044.
(56) Zheng, B.; Chen, T.-W.; Xiao, F.-N.; Bao, W.-J.; Xia, X.-H. KOH-activated Nitrogen-doped Graphene by Means of Thermal Annealing for Supercapacitor. *J Solid State Electrochem.* **2013**, *17*, 1809−1814.
(57) Qiu, B.; Pan, C.; Qian, W.; Peng, Y.; Qiu, L.; Yan, F. Nitrogen-doped Mesoporous Carbons Originated from Ionic Liquids as Electrode Materials for Supercapacitors. *J. Mater. Chem. A* **2013**, *1*, 6373−6378.
(58) Yang, X.; Zhuang, X.; Huang, Y.; Jiang, J.; Tian, H.; Wu, D.; Zhang, F.; Mai, Y.; Feng, X. Nitrogen-enriched Hierarchically Porous Carbon Materials Fabricated by Graphene Aerogel Templated Schiff-base Chemistry for High Performance Electrochemical Capacitors. *Polym. Chem.* **2015**, *6*, 1088−1095.
(59) Lv, Y.; Gan, L.; Liu, M.; Xiong, W.; Xu, Z.; Zhu, D.; Wright, D. S. A Self-template Synthesis of Hierarchical Porous Carbon Foams based on Banana Peel for Supercapacitor Electrodes. *J. Power Sources* **2012**, *209*, 152−157.
(60) Chang, B.; Guo, Y.; Li, Y.; Yin, H.; Zhang, S.; Yang, B.; Dong, X. Graphitized Hierarchical Porous Carbon Nanospheres: Simultaneous Activation/Graphitization and Superior Supercapacitance Performance. *J. Mater. Chem. A* **2015**, *3*, 9565−9577.
(61) Zhao, H.; Wang, L.; Jia, D.; Xia, W.; Li, J.; Guo, Z. Coal Based Activated Carbon Nanofibers Prepared by Electrospinning. *J. Mater. Chem. A* **2014**, *2*, 9338−9344.
(62) Yi, H.; Wang, H.; Jing, Y.; Peng, T.; Wang, X. Asymmetric Supercapacitors Based on Carbon Nanotubes@NiO Ultrathin Nanosheets Core-shell Composites and MOF-derived Porous Carbon Polyhedrons with Super-long Cycle Life. *J. Power Sources* **2015**, *285*, 281−290.
(63) Lee, K. H.; Oh, J.; Son, J. G.; Kim, H.; Lee, S. S. Nitrogen-doped Graphene Nanosheets from Bulk Graphite Using Microwave Irradiation. *ACS Appl. Mater. Interfaces* **2014**, *6*, 6361−6368.
(64) Pan, Z.; Cao, F.; Hu, X.; Ji, X. A Facile Method for Synthesizing CuS Decorated Ti_3C_2 MXene with Enhanced Performance for Asymmetric Supercapacitors. *J. Mater. Chem. A* **2019**, *7*, 8984−8992.
(65) Oyedotun, K. O.; Momodu, D. Y.; Naguib, M.; Mirghni, A. A.; Masikhwa, T. M.; Khaleed, A. A.; Kebede, M.; Manyala, N. Electrochemical Performance of Two-dimensional Ti_3C_2-Mn_3O_4 Nanocomposites and Carbonized Iron Cations for Hybrid Supercapacitor Electrodes. *Electrochim. Acta* **2019**, *301*, 487−499.
(66) Jiang, Q.; Kurra, N.; Alhabeb, M.; Gogotsi, Y.; Alshareef, H. N. All Pseudocapacitive MXene-RuO_2 Asymmetric Supercapacitors. *Adv. Energy Mater.* **2018**, *8*, No. 1703043.
(67) Liu, H.; Hu, R.; Qi, J.; Sui, Y.; He, Y.; Meng, Q.; Wei, F.; Ren, Y.; Zhao, Y.; Wei, W. One-Step Synthesis of Nanostructured CoS_2 Grown on Titanium Carbide MXene for High-Performance Asymmetrical Supercapacitors. *Adv Mater Interfaces* **2020**, *7*, No. 1901659.
(68) Fu, J.; Li, L.; Yun, J. M.; Lee, D.; Ryu, B. K.; Kim, K. H. Two-dimensional Titanium Carbide (MXene)-wrapped Sisal-Like $NiCo_2S_4$ as Positive Electrode for High-performance Hybrid Pouch-type Asymmetric Supercapacitor. *Chem. Eng. J.* **2019**, *375*, No. 121939.
(69) Vaghasiya, J. V.; Mayorga-Martinez, C. C.; Vyskočil, J.; Sofer, Z.; Pumera, M. Integrated Biomonitoring Sensing with Wearable Asymmetric Supercapacitors Based on Ti_3C_2 MXene and 1T-Phase WS_2 Nanosheets. *Adv. Funct. Mater.* **2020**, *30*, No. 2003673.

https://doi.org/10.1021/acsami.2c02507
ACS Appl. Mater. Interfaces 2022, 14, 19534−19546